Perspective: Size selected clusters for catalysis and electrochemistry Ⓕ

Avik Halder, Larry A. Curtiss, Alessandro Fortunelli, et al.

COLLECTIONS

Ⓕ   This paper was selected as Featured

View Online   Export Citation   CrossMark

ARTICLES YOU MAY BE INTERESTED IN

A consistent and accurate ab initio parametrization of density functional dispersion correction (DFT-D) for the 94 elements H-Pu
The Journal of Chemical Physics **132**, 154104 (2010); https://doi.org/10.1063/1.3382344

A climbing image nudged elastic band method for finding saddle points and minimum energy paths
The Journal of Chemical Physics **113**, 9901 (2000); https://doi.org/10.1063/1.1329672

Atomically precise (catalytic) particles synthesized by a novel cluster deposition instrument
The Journal of Chemical Physics **140**, 174201 (2014); https://doi.org/10.1063/1.4871799

Perspective: Size selected clusters for catalysis and electrochemistry

Avik Halder,[1] Larry A. Curtiss,[1] Alessandro Fortunelli,[2,3] and Stefan Vajda[1,4,a)]
[1]*Materials Science Division, Argonne National Laboratory, Lemont, Illinois 60439, USA*
[2]*CNR-ICCOM, Consiglio Nazionale delle Ricerche, 56124 Pisa, Italy*
[3]*Materials and Process Simulation Center, California Institute of Technology, Pasadena, California 91125, USA*
[4]*Institute for Molecular Engineering, The University of Chicago, Chicago, Illinois 60637, USA*

Size-selected clusters containing a handful of atoms may possess noble catalytic properties different from nano-sized or bulk catalysts. Size- and composition-selected clusters can also serve as models of the catalytic active site, where an addition or removal of a single atom can have a dramatic effect on their activity and selectivity. In this perspective, we provide an overview of studies performed under both ultra-high vacuum and realistic reaction conditions aimed at the interrogation, characterization, and understanding of the performance of supported size-selected clusters in heterogeneous and electrochemical reactions, which address the effects of cluster size, cluster composition, cluster–support interactions, and reaction conditions, the key parameters for the understanding and control of catalyst functionality. Computational modeling based on density functional theory sampling of local minima and energy barriers or *ab initio* molecular dynamics simulations is an integral part of this research by providing fundamental understanding of the catalytic processes at the atomic level, as well as by predicting new materials compositions which can be validated in experiments. Finally, we discuss approaches which aim at the scale up of the production of well-defined clusters for use in real world applications. *Published by AIP Publishing.* https://doi.org/10.1063/1.5020301

I. INTRODUCTION

Clusters containing a well-defined number of atoms offer an ideal platform to study catalysis at the atomic level and can provide detailed fundamental insight into catalytic processes that may be hampered by the complexity of catalysts prepared by more conventional methods which typically yield particles with finite distributions in size and composition. Such small uniform particles can also be realistically treated using accurate computational methods such as density functional theory (DFT), not only to achieve a molecular-level understanding of their function but also to design new catalytic materials in an atom-by-atom fashion. Exploiting the advances in synthesis techniques, one can gain control over the size and composition of the catalysts at the atomic level. The size-selected clusters described in this paper are typically generated in the gas phase and, after mass selection, deposited on suitable support materials at well-defined surface coverage (i.e., metal loading),[1,2] an approach that transitions earlier fundamental gas-phase investigations of clusters[3] toward the field of heterogeneous catalysis research. These clusters can serve as models of the catalytic active site, containing a large fraction of under-coordinated atoms. The size- and composition-dependent properties of the clusters are also strongly modified by their interaction with the support. As an example, we can consider Cu clusters for which the size dependency in cluster oxidation[4] and their catalytic properties toward CO_2 conversion[5] undergo a trend-reversal between gas phase

compared to when deposited on supports. The support material and its morphology can have a significant influence on the character and performance of a cluster via charge transfer as well as affecting cluster stability.[6–10] Moreover, alloy clusters can be created, in which composition is manipulated on the atomic scale, creating compositions that are not found as stable species in bulk phases. Minor changes in size and composition such as the addition or removal of a single atom can have a substantial influence on the activity and selectivity of a reaction. Understanding catalytic processes on an atomic level can potentially lead to the development of more efficient and cost-effective processes. There have been multiple instances where the highly active cluster catalysts are able to process reactions in an environmentally benign condition under low temperature and pressure, compared to bulk and nanosized catalysts of identical materials.[2] Last but not least, individual clusters which contain only a handful of atoms have a high surface-to-volume ratio which, from an applications perspective, can offer an excellent and economic utilization of the metal loading.

Theoretical and computational methods have played and promise to continue playing an important role in this field.[11,12] In fact, not only do they offer a parallel advanced form of characterization that can be contrasted with and usefully complements experiment, but they are also uniquely able to explore high-energy intermediates or transient states which can be important in the catalytic pathway but could otherwise be ignored as they escape experimental characterization. Indeed, the dependence of catalytic activity of size-selected clusters on cluster size, support, and (alloy) composition have all been investigated and rationalized by simulations, and the detailed

a)Author to whom correspondence should be addressed: vajda@anl.gov

catalytic mechanisms unveiled in a number of examples.[11,13] In addition, systematic computational searches have also singled out the role played by the shell of adsorbates (reactants, intermediates, products), formed on the initially under-coordinated clusters under realistic reaction conditions, as a decisive factor in determining stability and catalytic properties of these subnanometer catalysts.[13,14]

This review is not intended to be, and cannot be, exhaustive, within the allocated space, of all the reactions that have been studied in the literature. In this perspective, we thus limit ourselves to examples for a selected range of reactions which utilized size-selected clusters and provided fundamental insights into the reaction mechanisms of CO oxidation,[15–18] CO_2 conversion,[5,19] dehydrogenation,[6,20] hydrogenation,[21,22] epoxidation,[23–25] electrochemical water splitting,[26–28] and Li–O_2 electrochemistry.[29] (For the interested reader, there is a number of other reactions on size-selected clusters, such as the selective cleavage of the C–O–C bond,[30] or the size-dependent oxidation and reduction of clusters,[4] or acetylene trimerization.[31]) As demonstrated in the showcased studies, the synergy between experiment and theory is instrumental to explain some of the crucial questions in the field of catalysis research, such as the dependence of performance on particle size and composition, as well as particle/support interactions. Finally, we will provide a discussion on the scale up techniques to achieve a crossover from these model lab-scale catalysts to industrial applications and outlook.

II. SIZE-SELECTED CLUSTER GENERATION

Size-selected clusters are typically synthesized by employing physical methods, in high vacuum systems where the clusters ions are generated using a gas-phase cluster ion source, a mass selector, and ion beam optics for collimation and transport of the size-selected cluster ions to the substrate where the cluster ions are deposited. The cluster ion source may consist of a DC (direct current) or RF (radio frequency) magnetron sputtering source for generating clusters using a plasma of Ar gas or Ar mixed with a low dose of reactive gas such as oxygen, methane, or hydrogen sulphide to prepare metallic clusters, or metal oxide, metal carbide, and metal sulfide composite clusters, respectively.[32–34] Here, the sputtered metal atoms are cryogenically cooled by collisions with He gas under pressure inside the aggregation region to generate clusters with a tunable size distribution.[35–40] Through operating dual or multiple magnetron sputtering devices independently in a gas-aggregation cell, it is also possible to create mixed clusters.[41,42] The ions exiting the aggregation region are subsequently transported using an ion guide, followed by ion beam optics for collimation and finally size-separated and deposited. The cluster beam containing ions of a specific size is then deposited on the substrate.[38] Typical cluster ion beam currents are between tenths and few nanoamperes, and the clusters are soft-landed on the supports with an impact energy tuned to <2 eV/atom. Other commonly used cluster generation sources include laser vaporization where a laser beam interacts with a rotating metal rod to create a plasma at the point of contact.[17,43,44] The carrier gas within the aggregation

chamber helps in cluster generation as well as transporting the atoms and clusters from the plasma to a vacuum region. Clusters of mixed composition can also be created through laser vaporization by seeding a reactive gas, such as oxygen or methane, in the carrier gas to form oxides and carbides. Furthermore, mixed clusters can be formed using binary alloy targets or a dual-rod configuration.[45,46] Electrospray ionization is another technique for introducing clusters into the gas phase and concomitantly ionizing these species.[47,48] A solution of the cluster precursor passes a capillary maintained at a high voltage is electrosprayed into a carrier gas forming a molecular beam of ions through supersonic expansion. The precursors are introduced to the gas phase where the cluster aggregation occurs, with ligands attached and subsequently fragmented to remove ligands according to the precursor and bias placed on the capillary.[49]

The sources discussed herein produce a wide distribution of cluster sizes, and a mass separation technique is necessary to select a cluster of well-defined composition. Commonly utilized methods for size selection of charged particles are time of flight mass spectrometers (TOF MS),[37] radiofrequency quadrupole mass filters,[50] and electrostatic quadrupole mass filters.[51]

Typical supports used for cluster deposition are of model and technological relevance, such as oxide crystals and crystalline oxide films, oxide films prepared by atomic layer deposition (ALD) or carbon-based, for example, amorphous carbon, ultrananocrystalline diamond (UNCD), and highly ordered pyrolytic graphite (HOPG). The level of surface coverage of the support with clusters, typically at a fraction of atomic monolayer (ML) equivalent, is controlled by monitoring the flux of charged clusters landing on the support during deposition using a picoammeter. The known amount of deposited material can be then used in the determination of the activity on per cluster or atom basis. After deposition, the cluster samples are characterized and tested in gaseous or liquid environments, under ultra-high vacuum (UHV) conditions and realistic reaction conditions.

III. THEORETICAL TOOLS AND TECHNIQUES

The theoretical approach nearly universally utilized thus far in this field is density functional theory (DFT), in one of its several flavours. DFT in fact realizes an optimal compromise between the accuracy and computational effort. Simulations on systems composed of many tens up to few hundreds atoms are nowadays routinely performed on clusters of workstations or high-performance computing systems, thus enabling a realistic description of the composite aggregate formed by the metal clusters, the surrounding shell of ligands/adsorbates, and a piece of the support, then embedded into appropriate boundary conditions simulating the rest of the substrate.[52] The choice of the exchange-correlation (xc-)functional most appropriate for the system at hand is decisive for the predictive accuracy of the DFT approach. Importantly, such a choice can be guided and validated using sophisticated and computationally more demanding post-Hartree-Fock methods.[53,54] In general, it can be recalled that the development of more efficient and powerful architectures[55,56] promises a much increased accuracy

and reliability, and therefore an even more brilliant future to theoretical and computational research.

Using DFT approaches, local energy minimizations and frequency calculations can be performed first, hence predicting equilibrium geometries and energetics and validating the stability of investigated configurations. The potential energy surface connecting these local minima configurations can then be explored, hence locating the saddle points separating the basins of attraction corresponding to the local minima. Once the network of local minima and connecting saddle points is available, transition-state theory[57] can then be used to predict reaction rates among local minima, which can be inserted into a kinetic Monte Carlo algorithm[58] to model the complete catalytic process; see, e.g., Ref. 16 for a recent application of this strategy. Clearly, which configurations to select for investigation represents an open and difficult question. Despite the limited number of atoms directly involved in catalysis, structural sampling is in fact a non-trivial issue, not only because unusual atomic (geometric) arrangements can arise in the metal cluster, or the adsorbates, or the support (especially when considering amorphous systems) but also because the stoichiometry of the system at each given catalytic step is not defined *a priori* but rather results from steady-state reaction kinetics under the given experimental conditions. This leads to an exponential increase in the degrees of freedom to be explored.[59] To address this issue, global optimization techniques can be utilized,[60] i.e., systematic searches in the phase space of geometric configurations and stoichiometry, but to be really effective they should be improved and made more appropriate by combining systematic search with real-time evaluation of reaction rates then used to orient the system evolution according to the given experimental conditions, as, e.g., in the reactive global optimization approach.[12]

The techniques just described are very effective for dealing with systems exhibiting rugged potential energy surfaces (i.e., high energy barriers). In contrast, when the barriers among minima in the energy landscape are comparable with the thermal energy, it makes less sense to define a set of local minima configurations as basins of attraction, and, as an alternative strategy, *ab initio* molecular dynamic (AIMD) is a more appropriate technique to describe the dynamics and follow the structural evolution in real time of fluxional systems; see, e.g., Ref. 61 for a recent example. AIMD can also be used in general in combination with various acceleration techniques[62,63] to investigate chemical reactions, or simply as a test of the stability of a given configuration with respect to disaggregation and/or diffusion.[14]

IV. HETEROGENEOUS CATALYSIS

A. CO oxidation

1. CO oxidation on alumina-supported Pt$_{10}$, Ag$_9$Pt$_2$, and Ag$_9$Pt$_3$ clusters

Size-selected Pt$_{10}$, Ag$_9$Pt$_2$, and Ag$_9$Pt$_3$ clusters were deposited on ultrathin amorphous alumina support prepared by ALD, and tested under realistic conditions. The CO oxidation activity of all three cluster species tested was among the highest reported[15,16] with a turnover rate (TOR) between 250

and 300 molecules per second per metal atom at 300 °C, as shown in Figs. 1(a) and 1(b). However, at the highest applied temperatures, some decay in the activity was observed for the Pt$_{10}$/alumina sample. This decay was explained by STM characterization of Pt$_{10}$ clusters supported on crystalline alumina [Fig. 1(a)] due to a partial immersion of clusters into the alumina support as observed during the course of the reaction and/or poisoning by oxidized species such as carbonate (CO$_3$).[15] The catalyst deactivation could be completely curbed by switching to bimetallic Ag/Pt clusters Ag$_9$Pt$_2$ and Ag$_9$Pt$_3$, as confirmed from combined *in situ* grazing incidence small angle X-ray scattering/temperature programmed reactivity (GISAXS/TPRx) measurements [Fig. 1(b)].[16]

The Pt$_{10}$ system also made it possible, importantly, to clarify the crucial role of amorphous supports in stabilizing ultra-small clusters in heterogeneous catalysis.[15] First, Pt$_{10}$ clusters were deposited on a regular ultrathin alumina film grown on the NiAl(110) surface, which is a crystalline-line phase widely used as a surface science model of alumina. As a crucial point, this crystalline-like film, when subjected to the CO oxidation reaction under conditions identical to those held on the ALD-alumina support, was shown to convert to an amorphous phase apparently similar and in all analogous to the ALD-prepared film. Second, the Pt$_{10}$ clusters deposited on the ALD-alumina support did not show any sign of diffusion nor sintering even at elevated temperatures, in stark contrast with the same clusters deposited on a regular titania surface, which underwent reaction-induced cluster ripening and thus fast deactivation.[64]

DFT calculations [Fig. 1(c)] reveal the details of the potential energy landscape of bare and CO/O$_2$-covered Pt$_{10}$ clusters, predicting a 3D structure for Pt$_{10}$, an energy barrier of ~58 kJ mol^{-1} for CO oxidation, and an intermediate Pt oxidation state, in excellent agreement with the findings from the experimental reactivity and GIXANES (grazing incidence X-ray absorption near edge spectroscopy) characterization. The calculations also reveal a pressure (i.e., reactant coverage) dependent localization of the reaction from a top site to an interfacial one. In the case of Ag/Pt bimetallic clusters, the Pt atoms were found to anchor the mixed clusters to the support and to bind and activate two CO molecules, while Ag binds and activates O$_2$. In the bimetallic clusters, the proximity of Ag and Pt disfavors poisoning by CO or oxidized species such as carbonate (CO$_3$). As shown in Fig. 1(d), in the low temperature (RT) regime, the reaction proceeds via sequential co-adsorption of CO and O$_2$, formation of an OOCO oxametallocycle (OXA) which turns first into a CO$_3$ carbonate, after which a further adsorbed CO reacts with the carbonate to sequentially evolve two CO$_2$ molecules. At high temperature, the O$_2$ adsorption energy is not large enough to overcome the loss of entropic (translational) free energy, and Langmuir-Hinshelwood (LH) steps involving O$_2$ adsorption are replaced by Eley-Rideal (ER) steps.[16]

Notable in all Pt$_{10}$, Ag$_9$Pt$_2$, and Ag$_9$Pt$_3$ cases is that the reaction pathways proceed on a ligand/cluster/support complex exhibiting multiple adsorbed ligands (high coverage) as the catalytically active species. This feature has been advocated as a general phenomenon in heterogeneous catalysis by subnanometer clusters,[12,13,65] and the catalytic complex
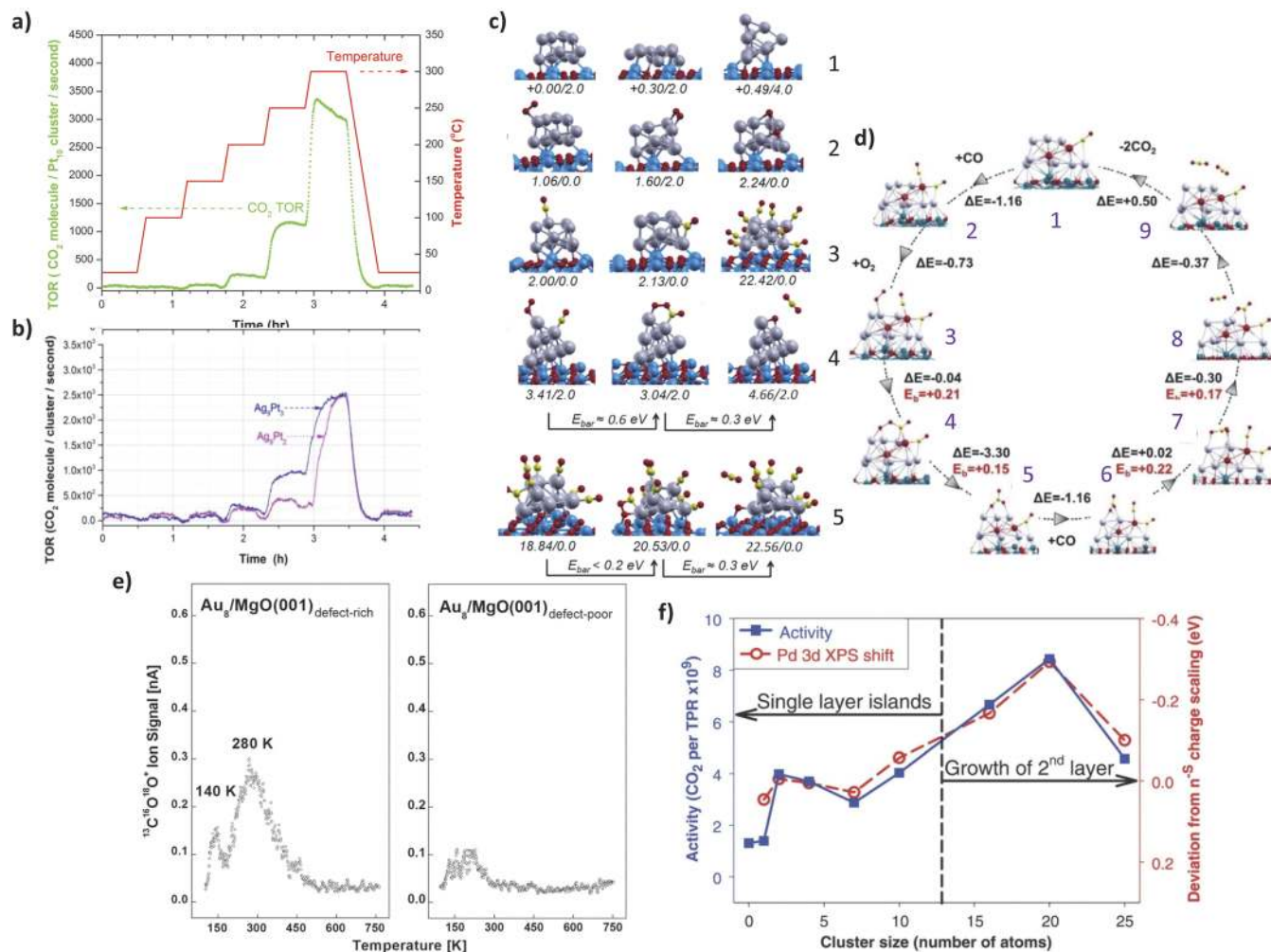
FIG. 1. CO oxidation using size-selected clusters on oxide supports. (a) Temperature ramp applied (solid line) during the CO oxidation reaction with the Pt_{10}/Al_2O_3 sample, and per cluster turnover rate as a function of temperature (dotted line). (b) Per cluster turnover rate of CO_2 formed on Ag_9Pt_2 (pink) and Ag_9Pt_3 (blue) clusters as a function of temperature. (c) (c1) Relative energies/total spin of the most stable structures of Pt_{10}/Al_2O_3. (c2-4) Adsorption energies/total spin of (c2) O_2, (c3) CO, and (c4 and c5) CO + O_2 species on Pt_{10}/Al_2O_3. In c4 and c5, the energy barriers of selected adsorption and reaction processes are also reported as E_{bar}. (d) Complete CO_{ox} catalytic cycle on Ag_9Pt_2 supported on the (001) surface of α-alumina. ΔE (in black) are reaction energies and E_b (in red) are reaction energy barriers. Langmuir-Hinshelwood (LH) steps ($2 \rightarrow 3 \rightarrow 4 \rightarrow 5$) hold at RT and are replaced by an Eley-Rideal (ER) step at high temperatures. Ag atoms are in gray, Pt atoms are in red, and O and Al atoms in the substrate are in small dark red and blue spheres, respectively. Energy values are in eV and spin in bohr. (e) Mass spectrometric signals pertaining to the formation of CO_2 on Au_8 deposited on F-center–rich MgO(001) thin films and on F-center–free MgO(001) thin films. To unambiguously show that both CO and O_2 are involved in the reaction, isotopically labeled ^{13}CO and $^{18}O_2$ were used. (h) CO oxidation activity observed during TPR (left axis, solid squares) with Pd_n clusters compared with shifts in the Pd 3d binding energy, relative to expectations from smooth bulk scaling (right axis, open circles), as a function of cluster size. (a) and (c) are adapted with permission from Yin *et al.*, J. Mater. Chem. A **5**, 4923 (2017). Copyright 2017 Royal Society of Chemistry. (b) and (d) are adapted with permission from Negreiros *et al.*, Angew. Chem., Int. Ed. **57**, 1209 (2018). Copyright 2017 Wiley-VCH Verlag GmbH & Co. KGaA. (e) is adapted with permission from Yoon *et al.*, Science **307**, 403 (2005). Copyright 2004 American Association for the Advancement of Science. (f) is adapted with permission from Kaden *et al.*, Science **326**, 826 (2009). Copyright 2005 American Association for the Advancement of Science.

thus *in situ* formed has been proposed as the proper analog of the metal complexes used in homogeneous catalysis.[66]

2. CO oxidation on size-selected Au and Pd clusters on oxide supports

Engineering defects on the substrates could provide a new route for increasing the activity of small deposited clusters. The following measurements have been performed under ultra-high vacuum (UHV) conditions, by investigating size-selected small gold octamers (Au_8) softlanded on a well-characterized crystalline MgO(001) surface prepared with and without oxygen vacancies. The Au_8 cluster deposited on the defect-rich magnesia surface was found active in oxidizing

CO into CO_2 at temperatures as low as 140 K. The same cluster bound to an MgO surface without oxygen vacancies (defect-poor) was catalytically inactive in CO combustion, as shown in Fig. 1(e). The experimental results supported by quantum-mechanical *ab initio* simulations show that the (i) the defect sites serve to anchor the deposited clusters more strongly than the defect-free surface and (ii) the defect sites also alter the charge state of the gold clusters leading to increased activity of the clusters through the promotion of the activation of the adsorbed reactant molecules by the formation of peroxo or superoxo species.[17] It should be added that oxygen vacancies have been claimed to be stabilized at the cluster/support interface and to play an

important role in CO oxidation via a Mars-van-Krevelen mechanism.[67]

The reactivity of the clusters is known to be strongly dependent on their electronic structure. X-ray photoemission spectroscopy measurements on soft-landed Pd clusters deposited on TiO_2 supports revealed that the Pd 3d binding energy varied non-monotonically with the cluster size and that the changes correlated with strong size variations in the CO oxidation activity, as shown in Fig. 1(f). The shift in the binding energy is a result of combined effects like charge transfer between the cluster and support, quantum confinement effects, and metal-metal bonding within the clusters. Electron transfer to the clusters has substantial effects on their ability to activate O_2, which is presumably the rate limiting step in the CO oxidation reaction. The left-hand axis shows the CO oxidation activity, given as the number of CO_2 product molecules desorbing during temperature-programmed reaction (TPR) from each sample. The low reactivity in the case of samples like Pd_1/TiO_2 and Pd_7/TiO_2 (and in context Pd_{25}/TiO_2) correlated with particularly stable valence structures.[18]

Several other important contributions toward the study of CO oxidation using deposited Ag,[68] Au,[69] Pd,[18,44,70,71] Pt,[72–74] and Rh[75] single element metallic clusters and also tin oxide clusters.[76] CO oxidation with bimetallic clusters like Ag–Au[65] and Co–Pt[77] has also been reported.

B. CO_2 conversion

Subnanometer-sized Cu_n clusters (n = 3, 4, and 20) provide a route to designing new catalysts for the efficient conversion of carbon dioxide.[78] The reduction and catalytic performance of the clusters was found strongly dependent on the cluster size. The temperature at which the initially oxidized clusters reduce decreases with increasing cluster size: Cu_3/Al_2O_3 > Cu_4/Al_2O_3 > Cu_{20}/Al_2O_3.[5] The onset of methanol production correlates with the reduction of Cu_n clusters (as determined by linear combination analysis of the X-ray absorption spectra), which suggests that the reduced phase of Cu catalysts plays a crucial role in the methanol synthesis from CO_2, as shown in Figs. 2(a) and 2(b).[5,19] The oxidation state of Cu clusters in Fig. 2(b) is obtained by performing a linear combination fitting of the XANES spectra of clusters with the XANES spectra of Cu bulk standards as discussed in detail in Ref. 5. Per copper atom methanol activity varies with the cluster size in the order of Cu_4/Al_2O_3
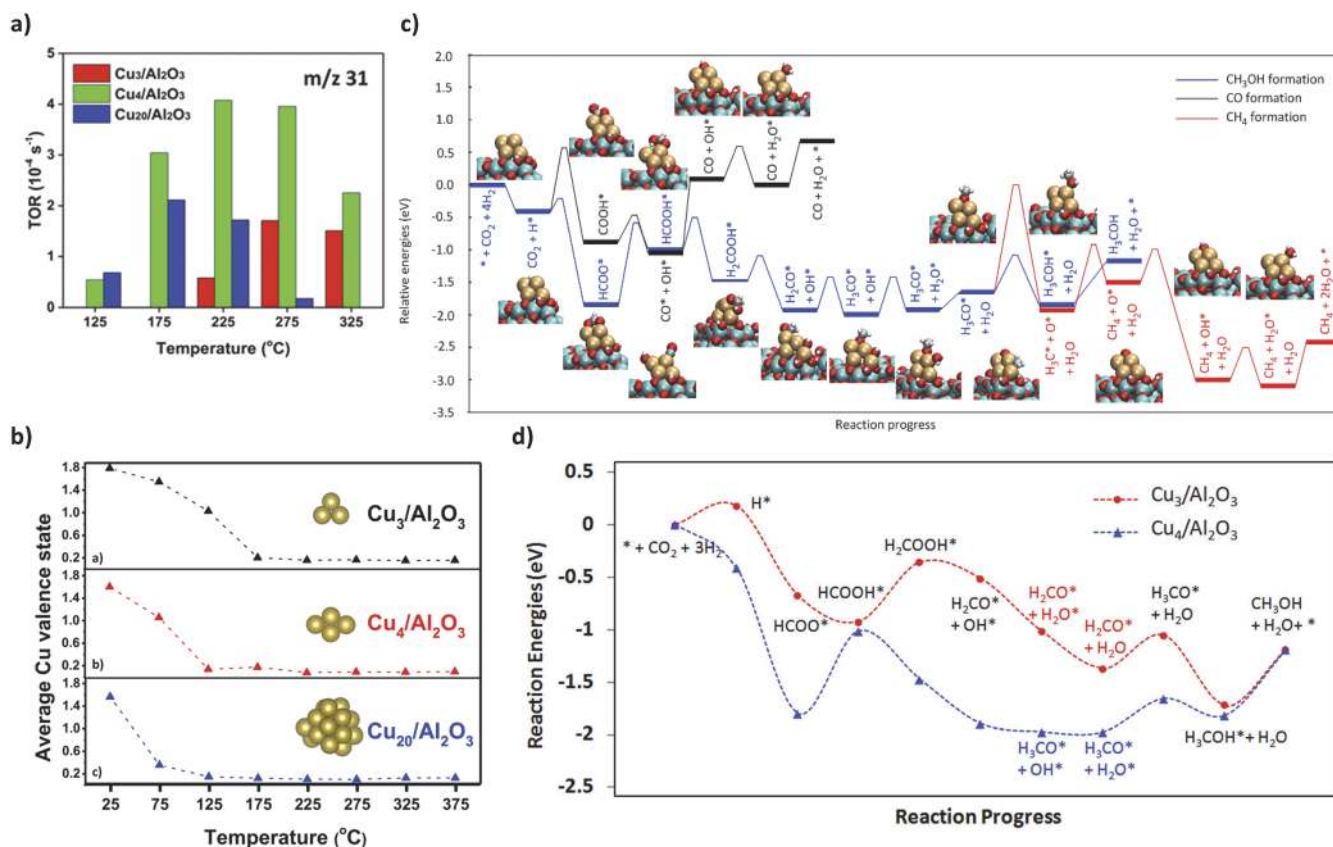

FIG. 2. Cu_n clusters in CO_2 conversion to methanol. (a) Methanol activity on Cu_3/Al_2O_3 (red), Cu_4/Al_2O_3 (green), and Cu_{20}/Al_2O_3 (blue) catalysts. The activity test was performed in a home-built flow reactor with 20 SCCM flow of 1% CO_2 and 3% H_2 gas mixture carried in helium at a pressure of 1.25 atm. The Cu_n catalysts were heated stepwise from 25 °C up to 425 °C under reaction conditions. The production rate of methanol (CH_3OH) was monitored at m/z 31 using a mass spectrometer. The turnover rate (TOR) was calculated by dividing the production rate of methanol molecules per second over total number of copper atoms in the catalyst. (b) Average Cu charge state of single-size copper catalysts with increasing reaction temperatures for Cu_3/Al_2O_3, Cu_4/Al_2O_3, and Cu_{20}/Al_2O_3. (c) Calculated reaction pathways of CO_2 reduction to CH_3OH, CO, and CH_4 on Al_2O_3 supported Cu_4 clusters. The catalyst surface site is labeled as "*". To improve legibility, "H_2" was omitted from the labels after the initial state. (d) Comparison of calculated reaction pathways of Cu_3 and Cu_4 clusters on hydroxylated Al_2O_3. (a), (b), and (d) are adapted with permission from Yang *et al.*, J. Phys. Chem. C **121**, 10406 (2017). Copyright 2017 American Chemical Society. (c) is adapted with permission from Liu *et al.*, J. Am. Chem. Soc. **137**, 8676 (2015). Copyright 2015 American Chemical Society.

> Cu_{20}/Al_2O_3 > Cu_3/Al_2O_3. As shown in Fig. 2(a), under low partial pressure of reactants (20 sccm flow of 1% CO_2 and 3% H_2 seeded in helium, at a total pressure of 1.25 atm), the methanol production reached its maximum around 225 °C at a turnover rate of about 4×10^{-4} methanol molecules per copper atom per second. The performance of this catalyst ranks among the most active for this reaction. By removing a single atom from Cu_4 to Cu_3, the rate of CH_3OH production drops dramatically, in excess of 50%. Above 325 °C, methane formation was also observed. The resulting reaction pathway from the predictive DFT calculations is shown in Fig. 2(c). The calculations predict that supported Cu_4 clusters have a very low activation barrier for conversion of CO_2 to CH_3OH resulting from strong binding of the adsorbates on the under-coordinated atoms of the copper clusters, resulting in an energetically lower-lying reaction pathway and a lower barrier.[19] The higher charge state of Cu in Cu_3/Al_2O_3 compared with Cu_4/Al_2O_3 leads to a weaker binding with intermediates, which is ultimately responsible for its lower per atom activity,[5] in contrary to the opposite size-dependent trend observed for gas-phase clusters. A similar reversal of trends between gas-phase and alumina-supported clusters has also been found for the oxidizability of free and alumina-supported clusters.[4]

C. Dehydrogenation of alkanes

Subnanometer Pt clusters deposited on alumina were found to be among the most active to dehydrogenate hydrocarbons; however, like many other catalysts, Pt may deactivate by coking in hydrocarbon-rich environments. Nanoalloying of Pt_7 with boron modified the cluster's alkene-(deuterated ethylene, C_2D_4) binding affinity and reduced its deactivation. The catalyst was prepared using size-selected deposition of Pt_7 clusters followed with the boration of the clusters by their exposure to diborane (B_2H_6).[79] Thought Pt_7 was more active than Pt_7B, boration made the cluster more stable as demonstrated by six sequential temperature programmed desorption/reaction (TPD/R) cycles under UHV conditions [Fig. 3(a)]. For Pt_7/Al_2O_3, the amount of both C_2D_4 desorbing and D_2 desorbing decreased substantially between the cycles, and post-reaction XPS showed significant carbon deposition.[79] For the borated Pt_7/alumina, the poisoning by coking was suppressed, no change was observed in C_2D_4 and D_2 desorption, and no carbon deposits were found by XPS. As shown in the accompanying calculations, boration lowers the binding energy of C_2D_4 such that desorption, rather than dehydrogenation and coking, is favored. CO TPD results shown in Fig. 3(b) revealed that for pure Pt_7, the number of CO binding sites is reduced dramatically after the first C_2D_4 TPD/R
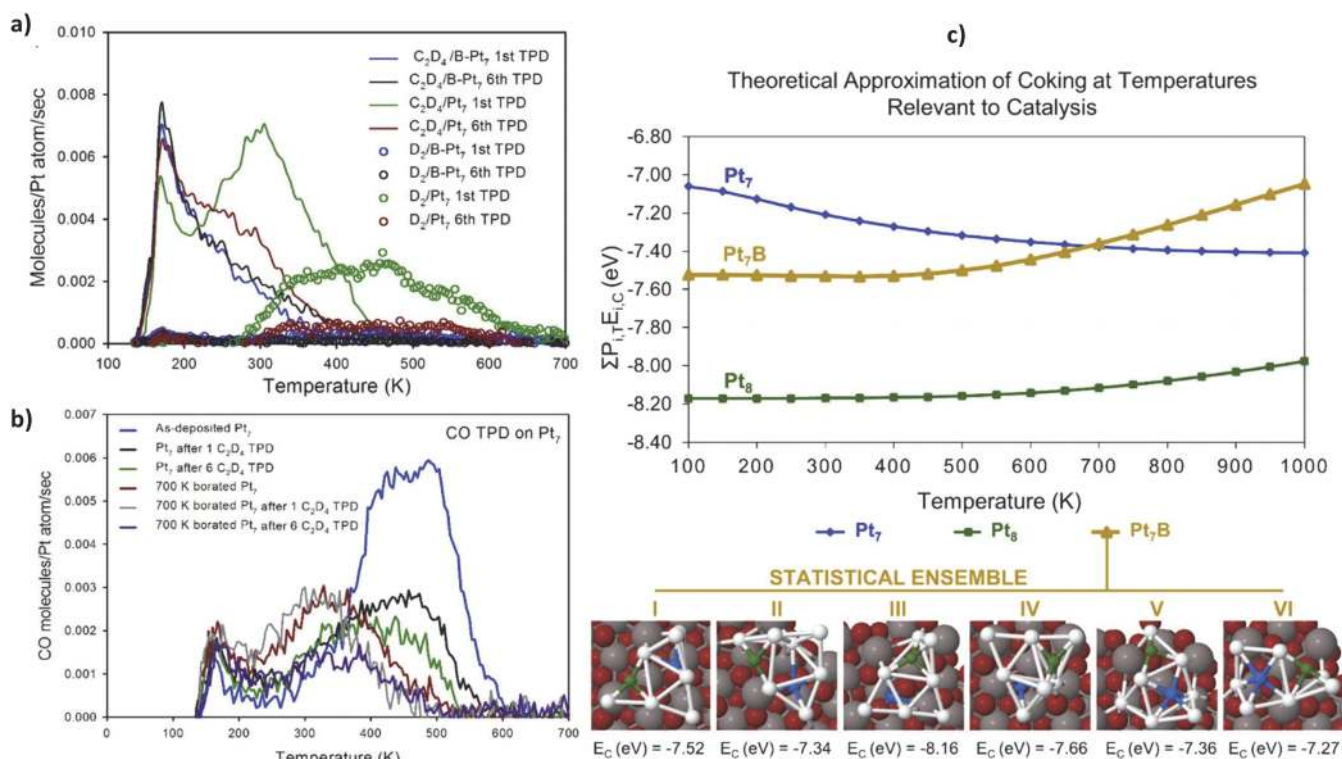

FIG. 3. Catalytic dehydrogenation on Pt_n and borated Pt_n clusters. (a) Intact C_2D_4 (solid) and D_2 (dots) desorbing from Pt_7/Al_2O_3 samples after various treatments: Pt_7 1st TPD/R run (green), Pt_7 6thC_2D_4 TPD/R run (dark red), borated Pt_7 1st TPD/R run (blue), and borated Pt_7 6th TPD/R run (black). (b) CO TPD from Pt_7 with different treatments: Pt_7 as-deposited (blue), Pt_7 after one C_2D_4 TPD/R run (black), Pt_7 after six C_2D_4 TPD/R runs (green), borated Pt_7 as prepared (dark red), borated Pt_7 after one C_2D_4 TPD/R run (gray), and borated Pt_7 after six C_2D_4 TPD/R runs (purple). The number of CO binding sites on pure Pt_7/alumina dramatically decreases after dehydrogenation, whereas borated clusters show fewer CO binding sites and shift toward weaker CO binding. (c) First-order approximation of coking: Boltzmann-weighted C-sticking energies for an ensemble. The Pt_7B isomers included in the ensemble are visualized at the bottom. As temperature rises, borated Pt exhibits increasing resistance to carbon. Boltzmann weights utilized as deposited Pt_7, Pt_8, and Pt_7B adsorption energies. Aluminum atoms are dark gray; oxygen, dark red; platinum, light gray; boron, blue; and carbon, green. Adapted with permission from Ha *et al.*, J. Am. Chem. Soc. **139**, 11568 (2017). Copyright 2017 American Chemical Society.

cycle and continued to drop during the six consecutive cycles, caused by a combination of coke deposition and cluster sintering/restructuring. The borated clusters also showed a gradual decrease in the number of CO binding sites in the sequential C_2D_4 TPD/R runs, which was most likely caused by the sintering of clusters as no C deposits are detected with XPS. MD calculations revealed smaller binding energies of Pt_7B to the support, which explained agglomeration, as well as a greater structural fluxionality of the borated clusters.[20] Boltzmann-weighted ensemble-averages of C-binding energies (E_C) of the isomers performed at 450 and 700 K for Pt_7, Pt_7B, and Pt_8 are shown in Fig. 3(c). Pt_8 was included in these calculations because it possesses prismatic isomers like Pt_7B. The temperature dependence of carbon affinity for Pt_7 and Pt_7B was found to have the opposite trend with temperature. For Pt_7, the ensemble-average E_C increases with temperature; that is, the population evolves to include more isomers with high carbon affinity. In contrast, for Pt_7B, higher energy planar configurations shown in Fig. 3(d) (isomers V and VI), in which B is exposed, rather than anchored to alumina (isomers I–IV), exhibit weaker E_C. As a result, the evolving ensemble for Pt_7B has decreasing carbon affinity and therefore increasing coke resistance as temperature rises. For Pt_8, E_C also decreases with temperature but remains much higher than that for Pt_7B. This

illustrates an important point that the size- and composition specific properties of cluster catalysts are necessarily ensemble averages and cannot be described by individual structures, even if they are the global minima.

Dehydrogenation of propane to propylene was highly active and selective on Pt_{8-10} clusters stabilized on high surface area supports made of commercial porous anodized aluminum oxide (AAO, Anopore) membranes coated with ALD (atomic layer deposition) alumina with an activity enhancement of up to 40–100 times compared to bulk Pt and vanadia based catalysts, studied under realistic reaction conditions.[6] Other examples of dehydrogenation reactions include the use of partially oxidized Co clusters in the oxidative dehydrogenation of cyclohexene, interrogated using various supports and reaction conditions.[9,80]

D. Hydrogenation of alkenes

Structure sensitivity may play a key role in some reactions of subnanometer clusters. Size-selected Pt_n (n = 8–15) clusters soft-landed on magnesia illustrated this propensity in the hydrogenation of ethylene to ethane under UHV conditions, accompanied by a parallel hydrogenation–dehydrogenation of the ethylidyne-producing route.[22] The TPR spectra for ethane production presented in Fig. 4(a) for Pt_n clusters show
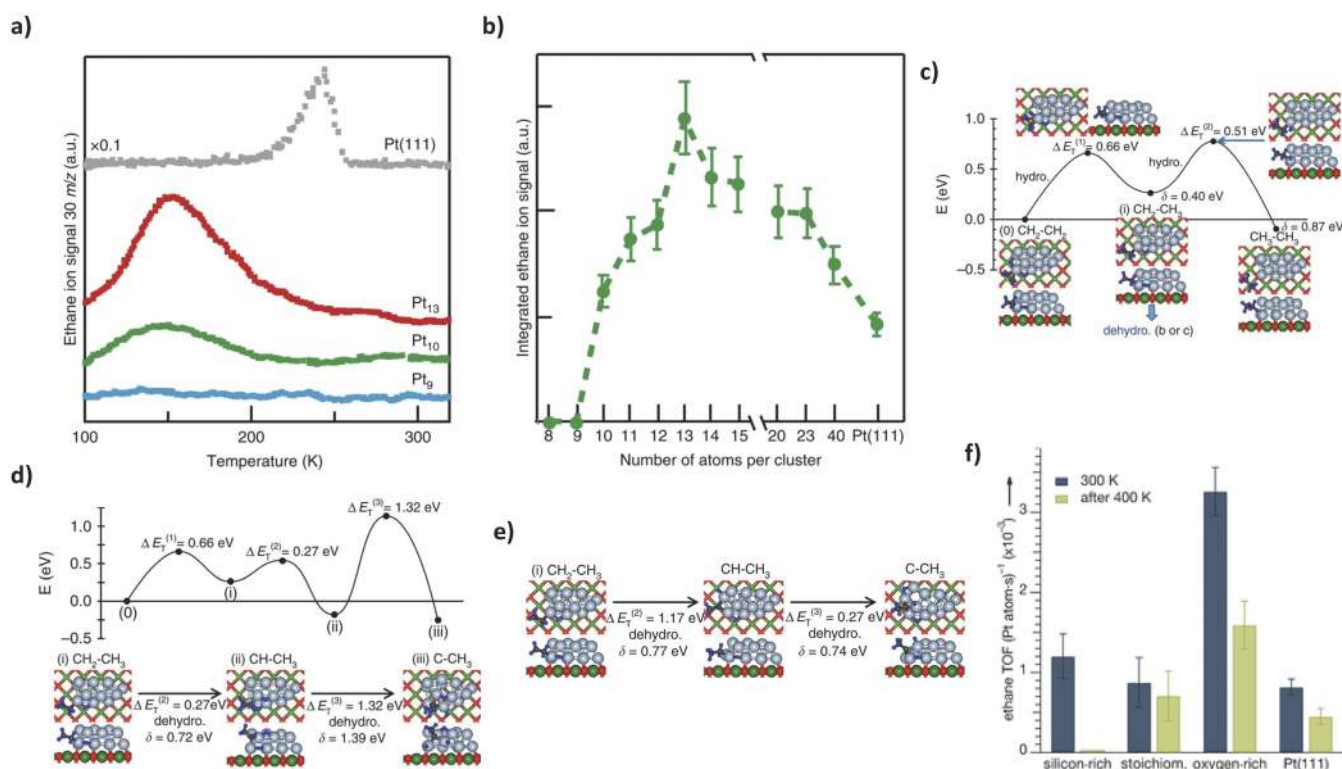

FIG. 4. TPR of ethylene hydrogenation on Pt_n clusters and Pt(111). (a) The measured ethane ion signals (m/z = 30) for Pt_9, Pt_{10}, Pt_{13}, and Pt(111) as a function of substrate temperature are shown. (b) The integrated signal from the curves in (a) as well as for cluster sizes up to Pt_{40} normalized to the number of Pt atoms is displayed. (c) Calculated first-principles steered reaction pathways catalyzed by Pt_{13}/MgO. Low-activation-barrier reaction pathway for hydrogenation of π-bonded ethylene configuration co-adsorbed with dissociated hydrogen on Pt_{13}/MgO. The reaction proceeds through the two successive hydrogenation steps described in the HP mechanism. The blue downward arrow near configuration (i) indicated the adsorbed ethyl intermediate (ii) is the starting configuration for the (d) and (e) pathways. [(d) and (e)] Alternative reaction channels yielding ethylidyne (C–CH$_3$), starting from the π-bonded ethylene configuration co-adsorbed with dissociated hydrogen [marked (0) in (c)]. (f) Ethylene hydrogenation kinetic data and IRRAS results with CO as a chemical probe before and after reaction. Pt_{13} TOF at 300 K as a function of SiO$_2$ support stoichiometry before (blue) and after (green) pulsing at 400 K. (a)–(e) are adapted with permission from Crampton *et al.*, Nat. Commun. **7**, 10389 (2016). Copyright 2016 Springer, Nature. (f) is adapted with permission from Crampton *et al.*, Angew. Chem., Int. Ed. **55**, 8953 (2016). Copyright 2016 Wiley-VCH Verlag GmbH & Co. KGaA.

negligible reactivity of the Pt_9 cluster, while a sizeable ethane production for Pt_{10} and Pt_{13} peaking at ~150 K, that is, ~100 K below the temperature measured on the extended Pt(111) surface. The results indicate similar activation energies for the clusters active in this size range which are considerably lower than the one found for the extended Pt(111) surface. The integrated areas under the measured TPR curves, normalized to the number of atoms per cluster, are shown in Fig. 4(b). This further illustrates that the supported platinum clusters catalyse the formation of ethane per Pt atom more efficiently than the Pt(111) surface. The Pt_{13} cluster was found to be the most active catalyst, with activity decreasing monotonically for cluster sizes both larger and smaller than Pt_{13}. The activity seized for clusters smaller than Pt_{10}. Extensive first-principles steered reaction-pathway (SRP) simulations have been done to gain insights into the microscopic ethylene hydrogenation mechanism. For Pt_9, no low-activation-energy hydrogenation channel was found in the simulations in agreement with the TPR results [Fig. 4(a)]. On the other hand, multiple reaction pathways, characterized by relatively low activation barriers, were found in SRP simulations for the larger clusters, as illustrated in Figs. 4(c)–4(e) for Pt_{13}. The simulated pathways starting from a π-bonded ethylene molecule co-adsorbed with a dissociated H_2 on the Pt_{13} cluster are shown in Fig. 4(c). For both cluster sizes, we observe that two successive energy barriers denoted as $\Delta E_T^{(1,2)}$ correspond to the two hydrogenation steps of the Horiuti-Polanyi (HP) mechanism, whose heights are sufficiently low to permit the experimentally observed low temperature. In addition to the low-activation-energy, pathways found on the Pt_{13}/MgO several reaction sites have been found which are characterized by higher ethylene-hydrogenation activation energy barriers; typically, ΔE_T > 0.8–1.0 eV. On Pt_{13}/MgO, multiple high-energy ethylidyne formation pathways are also shown in Figs. 4(c) and 4(d), manifesting energy-barriers of ΔE_T ~ 1.2–1.3 eV. This finding implies for Pt_{13} an onset of significant ethylidyne formation at high temperatures of ~350–400 K, which can poison the catalyst during ethylene hydrogenation.[22] Interestingly, previous theoretical studies of unsupported Pt_3 cluster had investigated the competition between π-bonded adsorption and σ-bonded adsorption of ethylene on small Pt clusters, suggesting that the former adsorption mode is favoured in the "coordinatively saturated" regime, whereas the latter is favoured in the "coordinatively saturated" regime, and that the energy barriers of reaction channels such as oxidative insertion of Pt into C–H bonds with the corresponding formation of platinum hydride species are lower in the latter regime, thus entailing a dependence of the interplay between hydrogenation and dehydrogenation upon ligand coverage.[81]

Further experiments have been performed to understand the effect of the thickness of the support thin film metal oxides on the morphology and chemical properties of Pt_{13} clusters. Thin amorphous silica films (a-SiO_2) were grown in UHV to obtain three types of a-SiO_2 films on a metal single crystal: silicon-rich, stoichiometric, and oxygen-rich.[82] The turnover frequency (TOF) of Pt_{13} was measured at 300 K (blue) as the function of the a-SiO_2 support stoichiometry using a pulsed molecular beam (PMB) technique,[83] as shown in Fig. 4(f). These results are compared with the TOF measured at 300 K

after pulsing a defined amount of ethylene at 400 K (green). A comparison is performed also with a Pt(111) single crystal. A distinct reactivity trend was observed before and after the 400 K step, which correlates with the support stoichiometry. At 300 K, the Pt_{13} clusters on both silicon-rich and stoichiometric films exhibit an activity comparable with the Pt(111) single crystal. However, the activity of the clusters increases three-fold in the oxygen-rich film. The next set of measurements was performed after pulsing a defined amount of ethylene at an elevated temperature of 400 K and the TOFs measured again at 300 K (green). A total deactivation is observed for the clusters supported on the silicon-rich film, while those on the oxygen-rich film lose about half their activity. No deactivation is found for the clusters supported on the stoichiometric film, while the Pt(111) single crystal loses some activity. First principles calculations provide insights into the structural and electronic characteristics of Pt_{13} clusters adsorbed on an a-SiO_2 surface.[21] The silicon-rich a-SiO_2 film donates electron density into the cluster, thereby filling unoccupied states closer to the Fermi level, and thus lowers the reaction barrier compared to the stoichiometric film. The complete deactivation of the activity at 400 K is caused due to a complete dehydrogenation of ethylene to ethylidyne and graphitic-like species. This is in marked difference with the oxygen rich film which withdraws electrons from the adsorbed clusters, causing a local shift in the energy levels which in turn increases the dehydrogenation activation barriers on Pt_{13} clusters. The enhanced activity at 300 K [Fig. 4(f)] is unprecedented as the ethylene hydrogenation is a structure insensitive reaction as found on the other two samples. At higher temperatures, the first dehydrogenated products start to form on the oxygen-rich support which results in a significant decrease in the activity observed after pulsing at 400 K.

Size-controlled Pd nanoparticles have also been used for the hydrogenation of furfural as shown in Ref. 84, while the influence of temperature and H_2 adsorption on the structure of silica-supported gold hexamer and heptamer clusters has been investigated in Ref. 85 with results in excellent agreement with experimental findings.

E. Epoxidation of alkenes

Three-atom silver clusters were softlanded at energies below 1 eV per silver atom on an amorphous ALD-alumina support. The stability of the clusters under reaction conditions was monitored *in situ* by grazing incidence small angle X-ray scattering (GISAXS) and their catalytic performance by using an in-line mass spectrometer, under atmospheric pressure. The Ag_3 clusters were found to undergo sintering at temperatures exceeding 120 °C [Fig. 5(a)], leading to the formation of stable aggregates (~2 nm tall, ~4 nm diameter). The dashed lines in Figs. 5(a)–5(c) indicate the onset temperature of the sintering of the silver trimers in a gas mixture of propylene and oxygen seeded in helium. The silver trimers showed an onset of propylene oxide formation already at temperatures as low as 50 °C, accompanied by the production of acrolein [Fig. 5(b)]. At higher temperatures, combustion to CO_2 prevailed, indicative of a highly efficient low-temperature activation of molecular oxygen on the silver trimer. Density functional theory (DFT) calculations
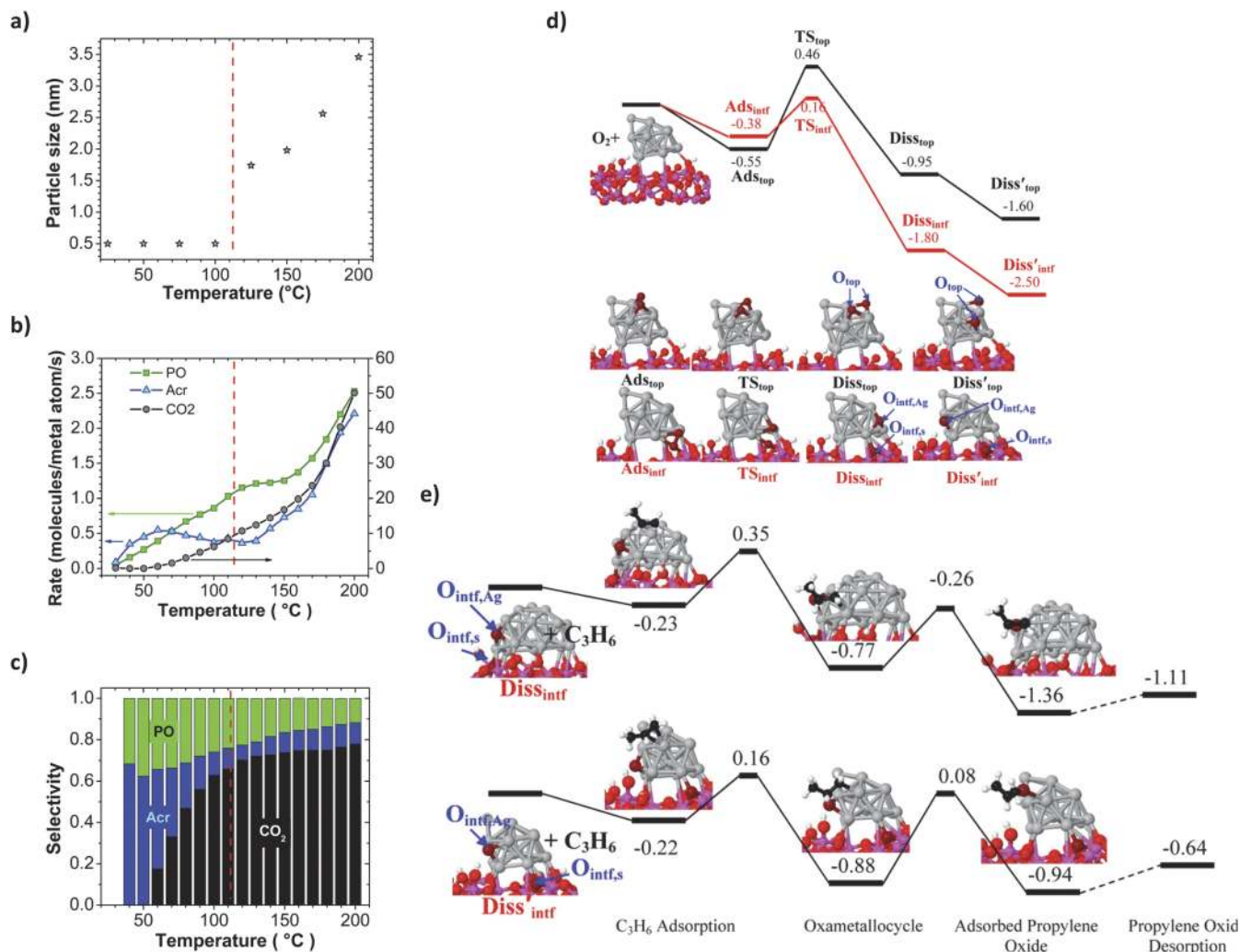
FIG. 5. Propylene oxidation using Ag_3 or Au_{6-10} clusters supported on thin oxide films. Ag_3 is supported on a ~3 monolayer thin amorphous alumina support prepared by atomic layer deposition on the top of a naturally oxidized n-type silicon wafer. (a) Average cluster size determined by *in situ* grazing incidence small-angle X-ray scattering (GISAXS) which reveals the onset of sintering of Ag_3 clusters above 120 °C. (b) Turnover rate of propylene oxidation toward propylene oxide (PO), acrolein (Acr), and CO_2 calculated per surface silver atom. (c) Selectivity of propylene oxide, acrolein, and CO_2 as a function of reaction temperature, showing the highest selectivity toward propylene oxide and acrolein at lower temperatures. The red vertical dashed lines in plots [(a)–(c)] indicate the onset temperature of the sintering of the Ag_3 clusters. (d) Reaction energy profile of O_2 dissociation on the alumina supported Ag_{19} interfacial (in red) and top site (in black). The size mimics the aggregates formed from Ag_3 in (a). Structures of O_2 adsorption (Ads), dissociation transition state (TS), and product of dissociation (Diss) are shown. More stable structures with two oxygen atoms apart from each other after O_2 dissociation are also shown (Diss′). Silver, oxygen, aluminum, and hydrogen atoms are shown in silver, red, magenta, and white, respectively. The two oxygen atoms from the O_2 molecule are shown in dark red for clarity. (e) Reaction energy profiles of propylene epoxidation on $O_{intf,Ag}$ sites of $Diss_{intf}$ and $Diss′_{intf}$ structures in (d). (a)–(c) are adapted with permission from Lei *et al.*, Science **328**, 224 (2010). Copyright 2010 American Association for the Advancement of Science. (d)–(e) are adapted with permission from Cheng *et al.*, ACS Catal. **4**, 32 (2014). Copyright 2014 American Chemical Society.

performed on the Ag_3/alumina system revealed the crucial role of the cluster–alumina support interface in the efficient activation of molecular oxygen on the Ag_3 cluster, as well as the role of atop and interfacial oxygen atoms in the epoxidation versus acrolein/CO_2 channel, respectively.[23] Ethylene epoxidation over Ag_3 clusters deposited on a different oxide support (MgO) has also been theoretically investigated, and high-coverage catalytic ligand/cluster/support complexes singled out for this reaction.[12,66]

To investigate the origin of high reactivity in Ag aggregates, O_2 dissociation and propylene epoxidation were studied on alumina-supported Ag_{19}.[24] The O_2 dissociation and propylene epoxidation apparent barriers at the interface between the Ag aggregate and the alumina support are calculated to be 0.2

and 0.2–0.4 eV, respectively as shown in Figs. 5(d) and 5(e), respectively. These barriers are somewhat lower than those on sites away from the interface. The mechanism at the interface is akin to what was found with silver trimer on alumina and can account for the high activity observed for the direct oxidation of propylene on the Ag aggregates. Due to lower barriers for oxygen dissociation at the interface and on the surfaces of the small Ag particles, the availability of oxygen is not the rate determining state, which is usually the case with crystalline surfaces.

Propene epoxidation has been also studied using Au clusters as catalysts and revealed an important role of hydrogen and water in tuning the activity and selectivity between the propylene oxide and acrolein formation.[86]

V. ELECTROCHEMISTRY

A. Water splitting

Co$_4$ and Co$_{27}$ clusters supported on a thin iron-oxide film made by ALD on the top of a Si wafer have been used to understand the role of individual catalytic sites in the complex water oxidation reaction.[87] Electrochemical and electrophotochemical measurements were performed at pH 13.6 to identify the oxygen evolution reaction (OER) activity of the samples. Figures 6(a) and 6(b) show the normalized linear sweep voltammetry (LSV) data taken under dark and illuminated (light) conditions for bare silicon, annealed Si/Fe$_2$O$_3$, and annealed Si/Fe$_2$O$_3$/Co$_{27}$ samples. The annealed Si/Fe$_2$O$_3$/Co$_{27}$ sample shows significantly improved electrochemical performance

under both dark and illuminated conditions. The photocurrents plotted in Fig. 6(c) show that neither the activity (dark) nor the photoactivity (light) of the thin Fe$_2$O$_3$ film changes after the annealing of the Si/Fe$_2$O$_3$ sample. The activity of the Si/Fe$_2$O$_3$/Co$_{27}$ sample was found to be three-fold higher than that of the (ALD)-deposited submonolayer Co film on a Fe$_2$O$_3$ support.[88] Also, the onset potential for oxidation under both dark and light remained unchanged for the Fe$_2$O$_3$ electrode. In brief, Co$_{27}$ clusters deposited at very low surface coverage on Fe$_2$O$_3$ anodes were significantly more active than Fe$_2$O$_3$ alone as a water oxidation catalyst in alkaline media, regardless of whether the anode is used as an electrocatalyst or as a photoelectrocatalyst. Grazing incidence X-ray absorption near-edge spectroscopy (GIXANES) characterization of
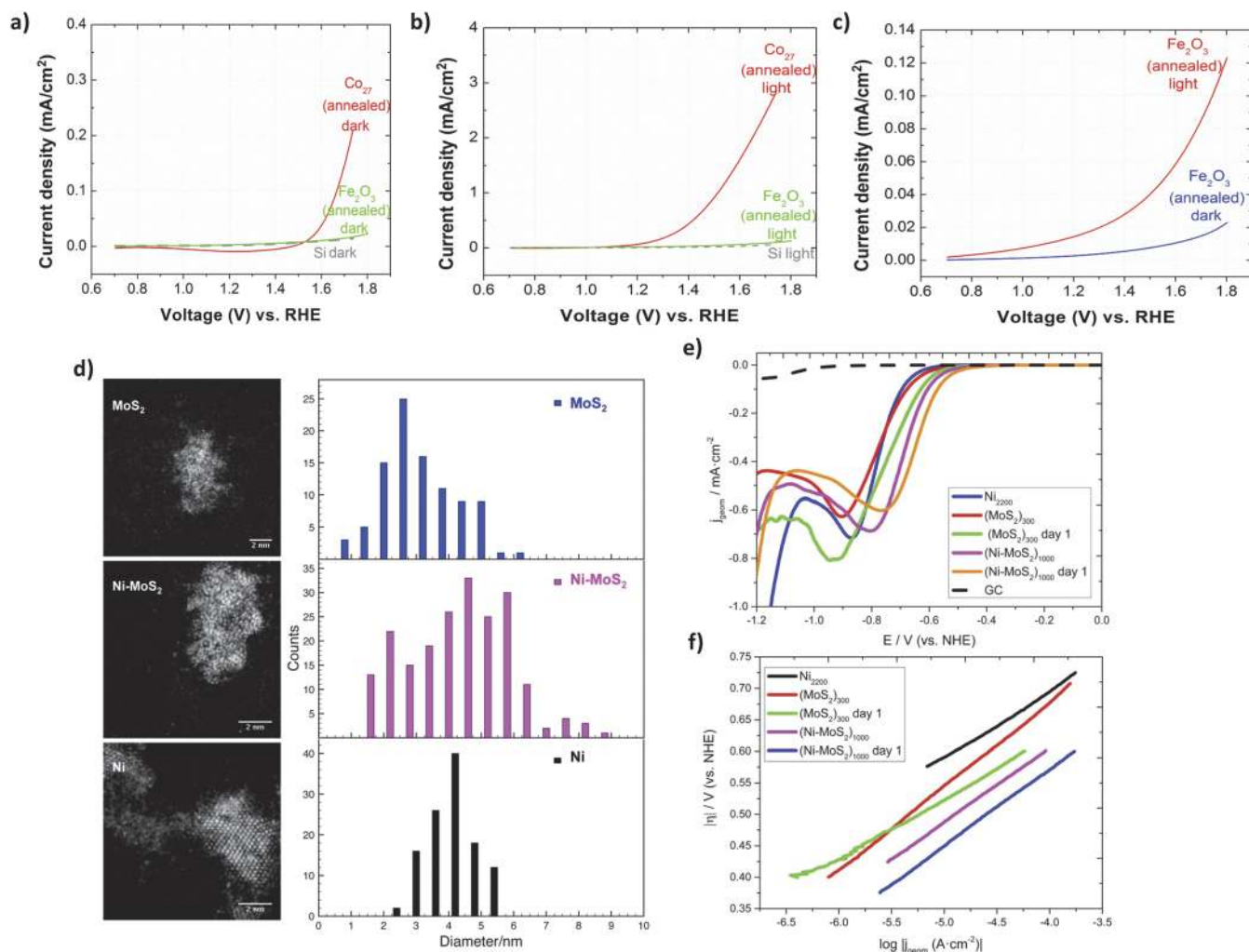

FIG. 6. Water oxidation using deposited Co$_n$ clusters and hydrogen evolution reaction using Ni cluster catalysts. Current density–voltage curves obtained on a Si electrode (grey dashed curve), annealed Si/Fe$_2$O$_3$ sample (green curve), and annealed Si/Fe$_2$O$_3$/Co$_{27}$ sample (red curve) in the dark (a) and under AM1.5G (Air Mass 1.5 Global spectrum) illumination (b). (c) Current density–voltage curves, normalized to the immersed area, obtained on the Si/Fe$_2$O$_3$ samples: (a) as-made Si/Fe$_2$O$_3$ sample in the dark and light and (b) annealed Si/Fe$_2$O$_3$ sample in the dark and light. Annealing of the Fe$_2$O$_3$ film does not enhance the oxidation current in the 2 nm-thin Fe$_2$O$_3$ films, within the estimated 15% uncertainty of the data. The voltage onset remains unchanged as well. One explanation for this behavior is improved charge-transport distances in the annealed films. (d) STEM images and size distribution in diameter based on the nanocluster surface area. MoS$_2$, Ni–MoS$_2$, and Ni have a peak value of 2.6, 5.0, and 4.2 nm, respectively. (e) Linear sweep voltammograms recorded at 5 mm diameter glassy carbon (dashed black) samples modified with fresh (MoS$_2$)$_{300}$ (solid red), fresh (Ni–MoS$_2$)$_{1000}$ (solid magenta), Ni$_{2200}$ (solid blue), 14-h air-exposed (MoS$_2$)$_{300}$ (solid green), and 14-h air-exposed (Ni–MoS$_2$)$_{1000}$ (solid orange) nanoclusters in the 0 to −1.2 V range vs normal hydrogen electrode (NHE). Scan rate: 25 mV s^{-1}. (f) Tafel plots (η vs log|j$_{geom}$|) of the Ni-doped/undoped MoS$_2$ nanoclusters evaluated in (e). Scan rate: 25 mV s^{-1}. (a)–(c) are adapted with permission from Pellin *et al.*, ChemSusChem **9**, 3005 (2016). Copyright 2016 Wiley-VCH Verlag GmbH & Co. KGaA. (d)–(f) are adapted with permission from Escalera-López *et al.*, ACS Catal. **6**, 6008 (2016). Copyright 2016 American Chemical Society.

the anodes before and after electro(photo)chemical cycling demonstrated that these Co_{27} clusters are stable to dissolution even in the harsh water oxidation electrochemical environment. It is hypothesized that in the annealed cluster sample $Si/Fe_2O_3/Co_{27}$ the much improved activity may be a result of a better charge transfer between the film and the cluster moiety.[26]

Other cluster based materials studied for electrochemical applications were transition metal dichalcogenides (TMDs). $Ni–MoS_2$ hybrid nanoclusters were prepared by the dual-target magnetron sputtering and gas condensation process.[27] The STEM images in Fig. 6(d) show (top to bottom) the morphologies of MoS_2 nanoclusters, $Ni–MoS_2$ hybrid nanoclusters, and Ni nanoclusters. A Z-contrast high angle annular dark field - scanning tunneling electron microscopy (HAADF-STEM) imaging has been performed to find the size distribution of the deposited nanoparticles. Figure 6(e) shows the linear sweep voltammograms acquired in the 0 to −1.2 V range [normalized vs normal hydrogen electrode (NHE)] at a scan rate of 25 mV s^{-1} in a 2 mM $HClO_4$/0.1M $NaClO_4$ aqueous electrolyte for all samples tested. The activity of $Ni–MoS_2$ hybrid nanoclusters is on par with previous reports of electrocatalytic enhancement to hydrogen evolution reaction (HER): an almost 3-fold increase in exchange current densities along with a significant shift in the onset potential (approximately 100 mV), compared to MoS_2 nanoclusters. The Tafel slope shown in Fig. 6(f) is almost unaffected ($\approx$120 mV dec^{-1}). The high activity is achieved when Ni is oxidized after the exposure of the samples to air. This has been further confirmed by XPS measurements.[27]

Studies with electrocatalytic water oxidation with sub-nanometer Pd[87] and Pt[89] clusters have also been studied in detail. The photocatalytic hydrogen evolution reaction with size-selected Pt clusters is presented in Ref. 90. Pt clusters have also been studied for oxygen reduction,[91–94] confirming an extreme dependence upon the precise size of the clusters[93] and ethanol electro-oxidation.[95]

B. Li–O$_2$ electrochemistry

Li–O$_2$ batteries are of great interest and provide a new concept of electric energy storage which involves an electrochemical formation of Li–O chemical bonds. These materials are a promising candidate for the long-range electric vehicles; however, its success relies on proper understanding of the charge and discharge chemistries.[29] Size-selected silver clusters of four sizes, Ag_3, Ag_9, Ag_{15}, and Ag_{18}, were deposited on alumina-passivated carbon support to study the effect of cluster size on the discharge process in Li–O$_2$ cells. Figures 7(a) and 7(b) show large and small area transmission electron microscopy (TEM) images of the electrode with deposited Ag_{15} clusters, showing evenly distributed and intact clusters, respectively. The study revealed dramatically different morphologies of the lithium peroxide (Li_2O_2) grown in cells depending on the size of the applied silver cluster. The resulting different nanoscale to microscale morphologies in the discharge product were understood to be due to the effect of the cluster size on the formation mechanism of lithium peroxide, which also affects the charge process. Out of the four

electrodes prepared with Ag_3, Ag_9, Ag_{15}, and Ag_{18} clusters, the electrode with Ag_{15} clusters possesses the largest charge capacity [Fig. 7(c)], moreover at the lowest charge potential of ~3.6 V [Fig. 7(d)]. Although the sizes of all clusters used were below a nanometer, their effect on the morphology of the micrometer-sized discharge products [Figs. 7(e)–7(h)], as well as on the nm-size building blocks of the discharge products [Figs. 7(i)–7(l)], was dramatic. The different morphologies of the Li–O$_2$ discharge products provide evidence, supported by detailed DFT calculations, for different discharge mechanisms which involve oxygen reduction followed by the formation of either lithium superoxide (LiO_2) or lithium peroxide (Li_2O_2) in the electrolyte, completed by surface nucleation and growth of the final discharge product from the electrolyte. The two discharge mechanisms proposed are either a fast oxygen reduction rate (ORR) as shown in Fig. 7(m) or a slow ORR as shown in Fig. 7(n). These explain the relation between the morphologies of the discharge products and different charge overpotentials with changing cluster size. This study of well-defined clusters on cathode surfaces provides evidence that the nature of the subnanometer surface species can strongly influence the morphology of the discharge products in Li–O$_2$ cells. These results imply that characterization of the surface structure of cathodes at an atomic/subnanometer level is a key factor in understanding the discharge and charge chemistries in lithium–air cells, and the tailoring of this structure is a potential avenue to improve the performance of Li–O$_2$ batteries.[29]

C. Electrocatalytic oxidation

Size-controlled gold clusters, here prepared by an alternative solution-based method, supported on functionalized carbon nanotubes demonstrated high catalytic activity toward the oxidation of thiophenol to disulphide in the presence of O_2.[96] Isolated gold atoms supported on functionalized multi-walled carbon nanotubes (MWCNTs) were synthesized by controlling the pH value of the medium and the concentration of the $HAuCl_4$ precursor. The aberration-corrected HAADF-STEM image of the sample is shown in Fig. 8(a). The TOF was measured as a function of time, and simultaneously samples were extracted at different time intervals which shows that the single atoms agglomerate to clusters and then to nanoparticles. The sample extracted after 6 min, immediately after the induction period when the catalytic reaction started to show the small cluster size of 4-13 gold atoms as presented in Fig. 8(b). After 120 min of reaction [Fig. 8(c)], the activity of the catalyst stopped. At this point, gold had aggregated into nanoparticles of diameter ≥2 nm. The population distribution as a function of time is shown in Fig. 8(d). For an alternative verification of the performance, isolated gold clusters with 3, 5–7, and 7–10 atoms were prepared separately and deposited on functionalized MWCNTs following the procedure described in Ref. 96 and the results are shown in Fig. 8(e). From these results, we can conclude that the most-active gold species for the oxidation of thiophenol to benzene disulfide correspond to small gold clusters that contain between five and ten atoms.[96] DFT calculations reveal that thiophenol adsorbs on all these clusters to form a stable Au–S bond and transfer charge from the S lone pair to metal LUMO. O_2 interaction with the clusters results in a noticeable activation of the O–O
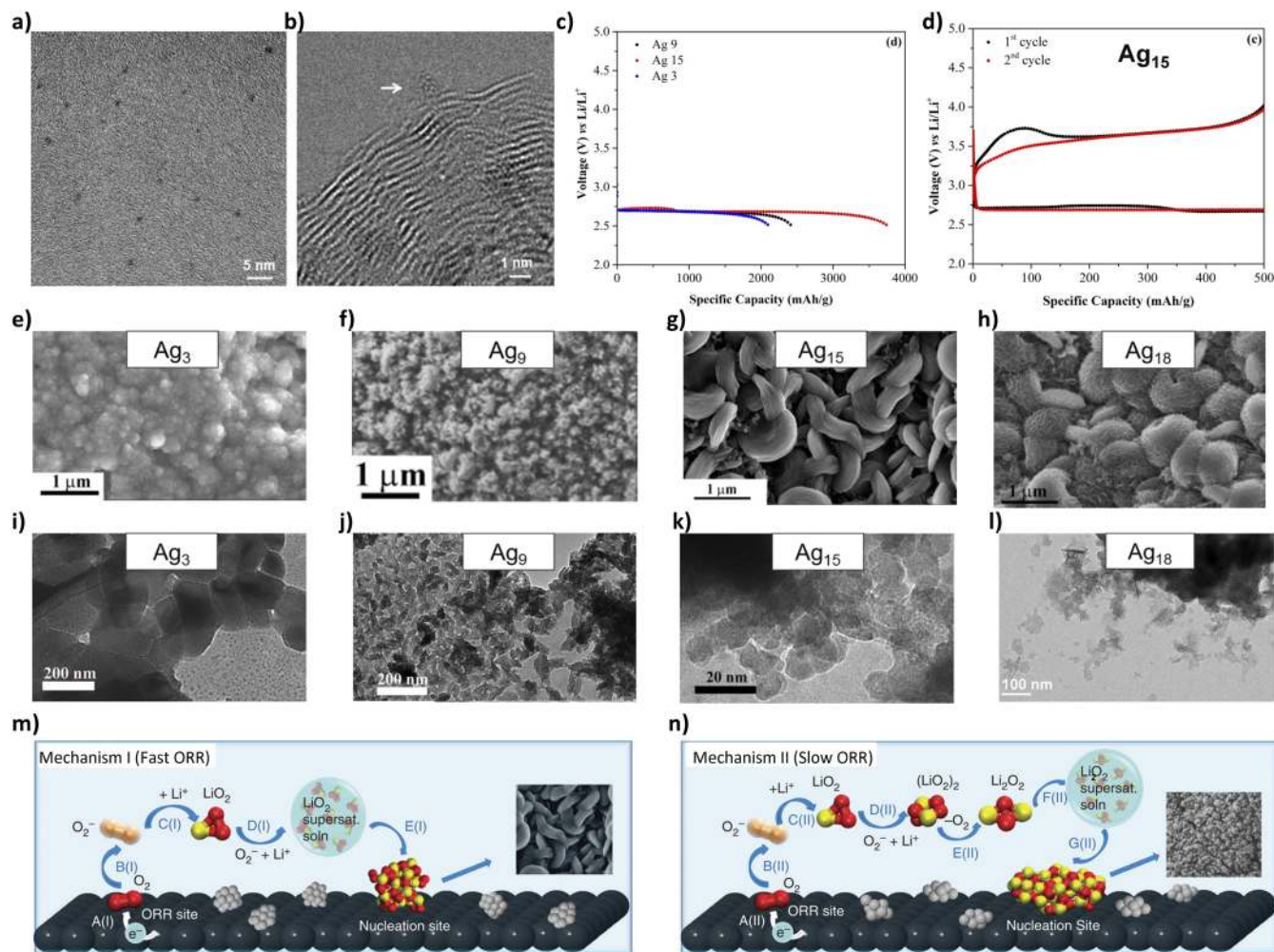
FIG. 7. Operational mechanism of a Li–O$_2$ cell studied using a size-selected cluster based cathode. (a) Large area transmission electron microscopy (TEM) image of 15-atom silver clusters on amorphous carbon support showing uniform distribution of clusters on the support. (b) High magnification TEM image of a Ag$_{15}$ cluster. (c) First discharge profiles of Ag$_3$, Ag$_9$, and Ag$_{15}$ based cathodes with a cutoff voltage of 2.5 V. (d) First two cycles of capacity controlled-voltage profiles of Li–O$_2$ cells using Ag$_{15}$ cluster based cathode materials. [(e)–(h)] SEM images of discharge products (discharge to 2.5 V) for Ag$_3$, Ag$_9$, Ag$_{15}$, and Ag$_{18}$ based cathode materials. [(i)–(l)] TEM images of discharge products (discharge to 2.5 V) on Ag$_3$, Ag$_9$, Ag$_{15}$, and Ag$_{18}$ based cathodes. (m) Proposed reaction mechanisms. Illustration of two discharge reaction mechanisms based on an initial oxygen reduction at an active site followed by solution phase reactions and growth at a surface nucleation site. (m) Mechanism I: step A: electron transfer to O$_2$; step B: O$_2$ desorption; step C: Li$^+$ reaction with O$_2$ to form solvated LiO$_2$; step D: repetition of steps A–C for LiO$_2$ formation to reach supersaturated LiO$_2$ solution; step E: surface nucleation and growth of LiO$_2$ that undergoes disproportionation. (n) Mechanism II: step A: electron transfer to O$_2$; step B: O$_2$ desorption; step C: Li$^+$ reaction with O$_2$ to form solvated LiO$_2$; step D: addition of O$_2$ and Li$^+$ to form LiO$_2$ dimer; step E: disproportionation to form Li$_2$O$_2$ and O$_2$; step F: repetition of steps A–E for Li$_2$O$_2$ formation to reach supersaturated Li$_2$O$_2$ solution; step G: surface nucleation and growth of Li$_2$O$_2$. Adapted with permission from Lu *et al.*, Nat. Commun. **5**, 4895 (2014). Copyright 2014 Nature Publishing Group.

bond as shown in Fig. 8(f). Coadsorption of thiophenol and O$_2$ is always energetically favourable, and in some cases a synergistic effect that leads to a higher degree of O$_2$ activation is observed. The reaction mechanism for Au$_5$ is shown in Fig. 8(g) which proceeds via coadsorption of thiophenol and O$_2$ on two neighbouring Au atoms, leading to the formation of H$_2$O$_2$ which eventually decomposes to two OH groups resulting in the formation of H$_2$O. After H$_2$O$_2$ desorption, the two thiolate fragments that remain adsorbed on the Au$_5$ cluster [Fig. 8(g)] are nearly neutral as shown in Fig. 8(h). Therefore, there is no electrostatic repulsion between the two S atoms, and the S–S bond can be formed that also involves an important rearrangement of the gold-cluster geometry. Au atoms and Au$_n$ clusters differ in the ability of the latter to

transfer electrons from thiolate fragments to O$_2$, which makes the formation of an S–S bond possible, as happens with sulfhydryl oxidase enzymes. For larger particles, a drop in the activity of disulphide formation is noticed as along with poisoning of the nanoparticles with thiolate groups. This is due to the lower concentration of active Au atoms accessible to reactants as particles grow, and by the strong Au–S interaction leading to the formation of very stable motifs and passivation of the gold nanoparticle surface [Fig. 8(i)].[97,98] However, the catalytic activity of size-selected unsupported thiol-protected metal clusters has been more closely investigated recently and shown in specific examples to be significant,[99] and thus the Au–S interactions may not always be detrimental to chemical activity.
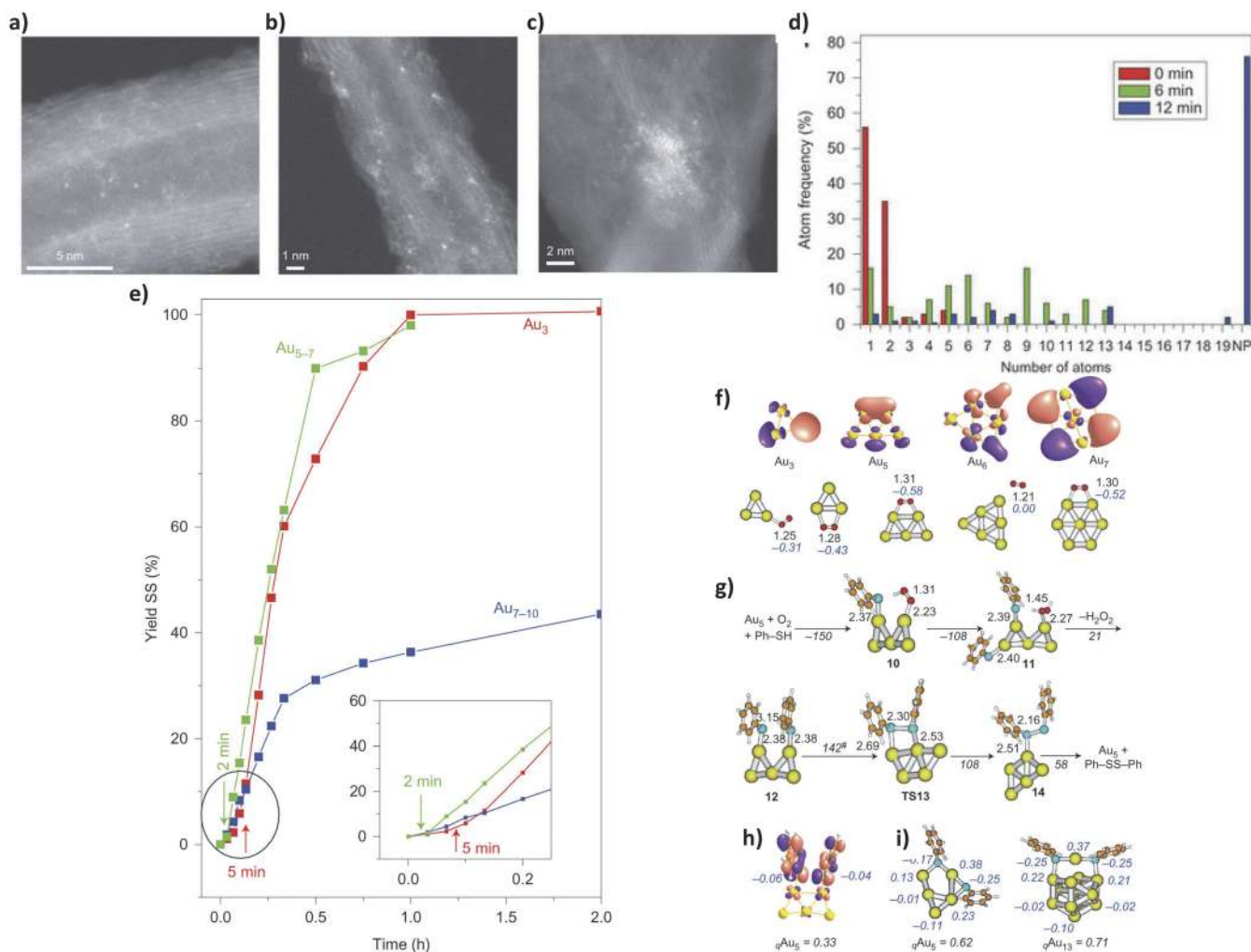
FIG. 8. Evolution of the gold species present on the catalyst and reactivity calculation. The evolution of gold species present on the catalyst was followed by stopping the reaction at different times, isolating the catalyst and characterizing it by means of HAADF-STEM. (a) Isolated gold atoms present on the as-prepared catalyst. (b) Image taken after 6 min shows the presence of small clusters with 4–13 atoms. (c) Images taken after 120 min of reaction, most of the gold aggregated into nanoparticles of diameter ≥ 2 nm. (d) Comparison of the atomic gold cluster distributions calculated for samples taken after different time intervals. (e) Oxidation of thiophenol to disulfide in the presence of O_2 catalysed by size-selected gold clusters. Gold clusters of Au_3, Au_{5-7}, and Au_{7-10} were synthesized by an electrochemical method and deposited on functionalized MWCNTs. Their activity was tested in the oxidation of thiophenol. Shown are the yields of disulfide versus reaction time using Au_3, Au_{5-7}, and Au_{7-10} gold clusters supported on MWCNTs as catalysts. (f) Atomic distribution of the HOMOs of Au_3, Au_5, Au_6, and Au_7 clusters, and optimized structures of the complexes formed by the interaction of these clusters with O_2. The numbers in black are the optimized O–O bond lengths (Å), and the numbers in blue are the net charge on O_2 in units of e. (g) Structures involved in the mechanism of disulfide formation catalysed by an Au_5 cluster. The numbers next to selected bonds are the optimized bond lengths (Å). The italic numbers beside the arrows are the reaction and activation (#) energies (kJ mol^{-1}) calculated for each elementary step. (h) Atomic distribution of the HOMO of structure 12. (i) Stable linear RS–Au–SR units, or "staple" motifs, formed over Au_5 and Au_{13} systems. The numbers in blue next to various selected atoms are net atomic charges in units of e. Gold, sulfur, carbon, oxygen, and hydrogen atoms are depicted in gold, blue, orange, red, and white, respectively. Figures are adapted with permission from Corma *et al.*, Nat. Chem. **5**, 775 (2013). Copyright 2013 Springer, Nature.

VI. ALTERNATIVE TECHNIQUES OF SIZE-SELECTED CLUSTER PRODUCTION AND SCALE UP

The model cluster systems that we have summarized in this perspective are ideal for a fundamental understanding of the catalytic properties, as well as well suited to identify new materials for chemical and electrochemical transformations, while they can also serve to validate the function of new materials designed by computational screening. However, most of the typical fabrication methods discussed so far that utilize physical gas phase production is designed for model/laboratory scale studies. These methods were not conceived with the goal to produce massive amounts of catalysts for industrial

applications. However, the very promising, and in several cases unique, properties of these cluster-based materials call for a scale up of their production. This has become an important endeavour, with some efforts utilizing the scale up of the very physical methods of size-selected cluster production through technical modifications,[100–105] and, very importantly also by employing alternative wet-chemical, solution-based methods to fabricate sizeable amounts of size-selected catalysts with very narrow size distributions,[96,106–108] also combining wet-chemical methods of a precursor that is then deposited and thermally decomposed to produce size-selected cluster catalysts supported on ionic surfaces such as zeolites[109] or anchored to carbon nanotubes.[110] However, in some cases, the ligand

effect might play a role in the catalyst performance.[111,112] Other advanced synthesis methods have been reported for ligand-free preparation of Ag,[113] Au,[96] and Ir[114] clusters, for example.

Recent development of new generations of cluster beam sources based on magnetron sputtering has successfully generated size-selected clusters of mass in the order of grams per hour.[100] This is several orders of magnitude higher than that produced in conventional cluster production sources that have been summarized above. The clusters are supported on (graphite) powders suitable for realistic test tube reaction conditions.[115] The catalyst powders were synthesized by cluster beam deposition onto the planar surface followed by microdicing. The catalysts are highly stable and sinter resistant. Performance of cluster-based catalysts has been compared with catalysts developed using the conventional "wet chemistry" technique. The catalysts have been tested for hydrogenation reactions which demonstrated great performance and in some cases outperform those synthesised following conventional methods.[100] There have also been other developed techniques like storing the clusters within a rare gas matrix.[101] Some other recent developments for cluster synthesis using a magnetron sputtering source include high-power impulse magnetron sputtering[104] or optimized design for generation of bimetallic and trimetallic alloy clusters.[102]

VII. CONCLUSIONS AND OUTLOOK

In the present review, we have tried to illustrate, via selected but representative showcase examples and accompanying discussion, the recent developments in the synthesis, experimental and theoretical characterization, and catalytic performance of size-selected subnanometer supported cluster catalysts.

A few key points can be derived from this overview.

First and foremost, the fact that these systems can exhibit an unconventional and sometimes extremely high catalytic activity and selectivity, so that they may rank among the most active catalysts reported to date and at the same time may be also viewed as models of the active site.

Second, the non-trivial dependence of the chemical properties of these systems on (i) their size/composition (such that adding or removing a single metal atom or replacing a single metal element with a dopant can dramatically alter their functions), (ii) the substrate on which they are deposited, and (iii) the reaction conditions (concept of ligand/cluster/support catalytic complex).

These two features make size-selected subnanometer clusters very promising and appealing systems in the search of novel, more active, and selective catalysts as required by present environmental and societal requirements, e.g., functioning under milder conditions of low temperature and pressure and/or minimizing the use of precious metals, as compared to bulk or nanosized catalysts of identical materials.

At the same time, because of these two same features, it is clear that some form of advanced characterization is necessary to shed light on reaction mechanisms and intermediates and thus to unveil and understand in depth the sometimes exotic chemistry of these systems, so as to fully realize their catalytic potential. Hence the important role played in recent advances by progress in both *in situ* experimental characterization techniques and in theory and computational modeling, for the unique capability of the latter to quantitatively test hypotheses of catalytic pathways and the associated sequence of configurations and transitions among them.

These combined and synergic experimental/theoretical studies clearly singled out the oxidation state of the metal elements (also depending on the charge transfer to/from the substrate and the adsorbates[116]) and the combined effect of the substrate and the ligand shell surrounding the cluster under realistic conditions, as two key factors determining catalytic behaviour. The ligand shell in fact operates together with cluster/substrate interactions to stabilize such small sub-nanometer and under-coordinated cluster species against disaggregation and/or diffusion over the substrate, leading to sintering and possible catalyst deactivation. In this respect, a crucial ingredient appears to be the amorphous character of the substrate, a fascinating subject but also extremely challenging in view of the issues it poses to both experimental characterization and theoretical (stochastic sampling) modeling.

The preceding discussion of the ligand effects naturally provides paths of future developments and progress as well. The importance of ligand high-coverage phases and of determining the ligand/cluster/support catalytic complex formed *in situ* under the environmental conditions of the specific catalytic reaction is one avenue which seems particularly fruitful and worthwhile elaborating. For example, the role played by catalyst preparation in real-world catalytic systems is well known, to a point that they often appear as "black magic" protocols.[117] In contrast to heterogeneous catalysis by larger nanoparticles where these techniques have been thoroughly investigated, such opportunities have not been emulated so far and are basically novel to the field of sub-nanometer catalysts. To quote one example, the use of a catalytic complex produced under the conditions of a given catalytic reaction as the catalyst in a different catalytic process has only been hypothesized or suggested theoretically but—to the best of our knowledge— never explored experimentally. Analogously, the introduction of additives and promoters into the reaction medium has not been explored so far, although it offers exciting perspectives especially once the details of the reaction mechanism have been appropriately revealed.

Another avenue which seems very promising is that of heterogeneous photo-catalysis. There is not so much knowledge on the optical properties of sub-nanometer supported metal clusters, see, e.g., Ref. 118, but it can be hypothesized, also by analogy with analogous size-selected systems,[119] that they can give rise to a rich photochemical behavior. Other unexplored avenue holding great potential is bond-selective electrochemical synthesis yielding gas, liquid, and solid phase products.

ACKNOWLEDGMENTS

[1]S. Vajda and M. G. White, ACS Catal. **5**, 7152 (2015).
[2]E. C. Tyo and S. Vajda, Nat. Nanotechnol. **10**, 577 (2015).
[3]Z. Luo, A. W. Castleman, and S. N. Khanna, Chem. Rev. **116**, 14456 (2016).
[4]N. Mammen *et al.*, Eur. J. Inorg. Chem. **2018**, 16.
[5]B. Yang *et al.*, J. Phys. Chem. C **121**, 10406 (2017).
[6]S. Vajda *et al.*, Nat. Mater. **8**, 213 (2009).
[7]K. Wettergren *et al.*, Nano Lett. **14**, 5803 (2014).
[8]C. Yin *et al.*, J. Phys. Chem. A **118**, 8477 (2014).
[9]S. Lee *et al.*, ChemCatChem **4**, 1632 (2012).
[10]S. Lee *et al.*, J. Phys. Chem. C **119**, 11210 (2015).
[11]G. A. Ferguson *et al.*, Top. Catal. **55**, 353 (2012).
[12]F. R. Negreiros *et al.*, Nanoscale **4**, 1208 (2012).
[13]F. R. Negreiros *et al.*, C. R. Chim. **17**, 625 (2014).
[14]L. Sementa *et al.*, Phys. Chem. Chem. Phys. **16**, 26570 (2014).
[15]C. Yin *et al.*, J. Mater. Chem. A **5**, 4923 (2017).
[16]F. R. Negreiros *et al.*, Angew. Chem., Int. Ed. **57**, 1209 (2018).
[17]B. Yoon *et al.*, Science **307**, 403 (2005).
[18]W. E. Kaden *et al.*, Science **326**, 826 (2009).
[19]C. Liu *et al.*, J. Am. Chem. Soc. **137**, 8676 (2015).
[20]M.-A. Ha *et al.*, J. Am. Chem. Soc. **139**, 11568 (2017).
[21]A. S. Crampton *et al.*, Angew. Chem., Int. Ed. **55**, 8953 (2016).
[22]A. S. Crampton *et al.*, Nat. Commun. **7**, 10389 (2016).
[23]Y. Lei *et al.*, Science **328**, 224 (2010).
[24]L. Cheng *et al.*, ACS Catal. **4**, 32 (2014).
[25]L. M. Molina *et al.*, Catal. Today **160**, 116 (2011).
[26]M. J. Pellin *et al.*, ChemSusChem **9**, 3005 (2016).
[27]D. Escalera-López *et al.*, ACS Catal. **6**, 6008 (2016).
[28]Y. Attia and M. Samer, Renewable Sustainable Energy Rev. **79**, 878 (2017).
[29]J. Lu *et al.*, Nat. Commun. **5**, 4895 (2014).
[30]W. Deng *et al.*, Appl. Catal., A **393**, 29 (2011).
[31]F. Maleki, P. Schlexer, and G. Pacchioni, Surf. Sci. **668**, 125 (2018).
[32]H. Haberland *et al.*, J. Vac. Sci. Technol., A **10**, 3266 (1992).
[33]H. Haberland, M. Karrais, and M. Mall, Z. Phys. D: At., Mol. Clusters **20**, 413 (1991).
[34]S. Pratontep *et al.*, Rev. Sci. Instrum. **76**, 045103 (2005).
[35]A. Halder, A. Liang, and V. V. Kresin, Nano Lett. **15**, 1410 (2015).
[36]A. Halder and V. V. Kresin, Phys. Rev. B **92**, 214506 (2015).
[37]B. van Issendorff and R. E. Palmer, Rev. Sci. Instrum. **70**, 4497 (1999).
[38]C. Yin *et al.*, J. Chem. Phys. **140**, 174201 (2014).
[39]S. P. Price *et al.*, Surf. Sci. **605**, 972 (2011).
[40]S. Duffe *et al.*, Nat. Nanotechnol. **5**, 335 (2010).
[41]F. Yin, Z. W. Wang, and R. E. Palmer, J. Am. Chem. Soc. **133**, 10325 (2011).
[42]H. Yasumatsu, Eur. Phys. J. D **63**, 195 (2011).
[43]H. W. Kroto *et al.*, Nature **318**, 162 (1985).
[44]W. E. Kaden *et al.*, J. Chem. Phys. **136**, 204705 (2012).
[45]W. Bouwen *et al.*, Rev. Sci. Instrum. **71**, 54 (2000).
[46]H. Häkkinen *et al.*, Angew. Chem., Int. Ed. **42**, 1297 (2003).
[47]M. R. Ligare, G. E. Johnson, and J. Laskin, Phys. Chem. Chem. Phys. **19**, 17187 (2017).
[48]A. Li *et al.*, Angew. Chem. **126**, 12736 (2014).
[49]G. E. Johnson, T. Priest, and J. Laskin, ACS Nano **6**, 573 (2012).
[50]P. E. Miller and M. B. Denton, J. Chem. Educ. **63**, 617 (1986).
[51]R.-P. Methling *et al.*, Eur. Phys. J. D **16**, 173 (2001).
[52]G. Barcaro and A. Fortunelli, J. Chem. Theory Comput. **1**, 972 (2005).
[53]X. W. Zhou, R. A. Johnson, and H. N. G. Wadley, Phys. Rev. B **69**, 144113 (2004).
[54]L. O. Paz-Borbón *et al.*, Phys. Rev. B **85**, 155409 (2012).
[55]I. S. Ufimtsev and T. J. Martínez, J. Chem. Theory Comput. **4**, 222 (2008).
[56]A. Kandala *et al.*, Nature **549**, 242 (2017).
[57]G. H. Vineyard, J. Phys. Chem. Solids **3**, 121 (1957).
[58]D. T. Gillespie, J. Comput. Phys. **22**, 403 (1976).
[59]P. Kirkpatrick and C. Ellis, Nature **432**, 823 (2004).
[60]R. Ferrando, A. Fortunelli, and R. L. Johnston, Phys. Chem. Chem. Phys. **10**, 640 (2008).
[61]Y.-G. Wang *et al.*, Nat. Commun. **6**, 6511 (2015).
[62]A. F. Voter, Phys. Rev. Lett. **78**, 3908 (1997).
[63]C. Junghans, D. Perez, and T. Vogel, J. Chem. Theory Comput. **10**, 1843 (2014).
[64]S. Bonanni *et al.*, J. Am. Chem. Soc. **136**, 8702 (2014).
[65]F. R. Negreiros *et al.*, ACS Catal. **2**, 1860 (2012).
[66]L. Sementa, G. Barcaro, and A. Fortunelli, Inorg. Chim. Acta **431**, 150 (2015).
[67]A. R. Puigdollers and G. Pacchioni, ChemCatChem **9**, 1119 (2017).
[68]P.-T. Chen *et al.*, J. Phys. Chem. C **121**, 6614 (2017).
[69]K.-J. Hu *et al.*, J. Am. Chem. Soc. **137**, 15161 (2015).
[70]M. D. Kane, F. S. Roberts, and S. L. Anderson, J. Phys. Chem. C **119**, 1359 (2015).
[71]W. E. Kaden *et al.*, J. Am. Chem. Soc. **132**, 13097 (2010).
[72]S. Bonanni *et al.*, J. Am. Chem. Soc. **134**, 3445 (2012).
[73]S. Bonanni *et al.*, ACS Catal. **1**, 385 (2011).
[74]P. Ferrari *et al.*, Angew. Chem., Int. Ed. **55**, 11059 (2016).
[75]I. S. Parry *et al.*, J. Phys. Chem. A **117**, 8855 (2013).
[76]Y. Inomata, K. Albrecht, and K. Yamamoto, ACS Catal. **8**, 451 (2018).
[77]B. Yang *et al.*, J. Phys. Chem. C **120**, 21496 (2016).
[78]D. Cheng *et al.*, ChemSusChem **6**, 944 (2013).
[79]E. T. Baxter *et al.*, ACS Catal. **7**, 3322 (2017).
[80]S. Lee *et al.*, Phys. Chem. Chem. Phys. **14**, 9336 (2012).
[81]G. Barcaro and A. Fortunelli, Theor. Chem. Acc. **123**, 317 (2009).
[82]A. S. Crampton *et al.*, J. Phys. Chem. C **119**, 13665 (2015).
[83]C. H. Hu *et al.*, J. Catal. **274**, 99 (2010).
[84]S. M. Rogers *et al.*, ACS Catal. **7**, 2266 (2017).
[85]G. Barcaro *et al.*, Comput. Theor. Chem. **1021**, 222 (2013).
[86]S. Lee *et al.*, Angew. Chem., Int. Ed. **48**, 1467 (2009).
[87]G. Kwon *et al.*, ACS Nano **7**, 5808 (2013).
[88]S. C. Riha *et al.*, ACS Nano **7**, 2396 (2013).
[89]A. von Weber and S. L. Anderson, Acc. Chem. Res. **49**, 2632 (2016).
[90]F. F. Schweinberger *et al.*, J. Am. Chem. Soc. **135**, 13262 (2013).
[91]A. von Weber *et al.*, J. Phys. Chem. C **119**, 11160 (2015).
[92]S. Proch *et al.*, J. Am. Chem. Soc. **135**, 3073 (2013).
[93]T. Imaoka *et al.*, J. Am. Chem. Soc. **135**, 13089 (2013).
[94]L. Sementa *et al.*, Catal. Sci. Technol. **6**, 6901 (2016).
[95]A. von Weber *et al.*, Phys. Chem. Chem. Phys. **17**, 17601 (2015).
[96]A. Corma *et al.*, Nat. Chem. **5**, 775 (2013).
[97]P. D. Jadzinsky *et al.*, Science **318**, 430 (2007).
[98]H. Häkkinen, Nat. Chem. **4**, 443 (2012).
[99]G. Li and R. Jin, Acc. Chem. Res. **46**, 1749 (2013).
[100]P. R. Ellis *et al.*, Faraday Discuss. **188**, 39 (2016).
[101]R. E. Palmer, L. Cao, and F. Yin, Rev. Sci. Instrum. **87**, 046103 (2016).
[102]L. Martínez *et al.*, Langmuir **28**, 11241 (2012).
[103]P. Grammatikopoulos *et al.*, Adv. Phys.: X **1**, 81 (2016).
[104]C. Zhang *et al.*, J. Phys. Chem. A **117**, 10211 (2013).
[105]M. L. Cicero *et al.*, J. Chem. Phys. **147**, 214706 (2017).
[106]Z. W. Seh *et al.*, Science **355**, eaad4998 (2017).
[107]J. Oliver-Meseguer *et al.*, Science **338**, 1452 (2012).
[108]N. Vilar-Vidal, J. Rivas Rey, and M. A. L. Quintela, Small **10**, 3632 (2014).
[109]J. Meurig Thomas *et al.*, Faraday Discuss. **138**, 301 (2008).
[110]A. Bruma *et al.*, Nanoscale **5**, 9620 (2013).
[111]J. Selva *et al.*, J. Am. Chem. Soc. **132**, 6947 (2010).
[112]H. Tsunoyama, Y. Negishi, and T. Tsukuda, J. Am. Chem. Soc. **128**, 6036 (2006).
[113]A. Baldansuren *et al.*, J. Phys. Chem. C **113**, 19623 (2009).
[114]J. F. Goellner, J. Guzman, and B. C. Gates, J. Phys. Chem. B **106**, 1229 (2002).
[115]V. Habibpour *et al.*, J. Exp. Nanosci. **8**, 993 (2013).
[116]G. Pacchioni, L. Giordano, and M. Baistrocchi, Phys. Rev. Lett. **94**, 226104 (2005).
[117]H.-J. Freund, "Clusters and islands on oxides: From catalysis via electronics and magnetism to optics," Surf. Sci. **500**, 271–299 (2002).
[118]T. Lunskens *et al.*, Phys. Chem. Chem. Phys. **17**, 17541 (2015).
[119]G. Barcaro *et al.*, Phys. Chem. Chem. Phys. **17**, 27952 (2015).